

Article

Electrochemical Performance of Orthorhombic CsPbI₃ Perovskite in Li-Ion Batteries

Nahid Kaisar ^{1,†}, Tanmoy Paul ^{1,†}, Po-Wei Chi ¹, Yu-Hsun Su ¹, Anupriya Singh ², Chih-Wei Chu ², Maw-Kuen Wu ¹ and Phillip M. Wu ^{3,*}

¹ Institute of Physics, Academia Sinica, Taipei 11529, Taiwan; nahid0kaisar@gmail.com (N.K.); paultanmoy00@gmail.com (T.P.); dr.pwchi@gmail.com (P.-W.C.); a810808a@gmail.com (Y.-H.S.); mkwu@phys.sinica.edu.tw (M.-K.W.)

² Research Center for Applied Science, Academia Sinica, Taipei 11529, Taiwan; anupriyas962@gmail.com (A.S.); gchu@gate.sinica.edu.tw (C.-W.C.)

³ Department of Materials and Mineral Resources Engineering, National Taipei University of Technology, Taipei 10608, Taiwan

* Correspondence: philwu@gmail.com

† They share equal authorship.

Abstract: A facile solution process was employed to prepare CsPbI₃ as an anode material for Li-ion batteries. Rietveld refinement of the X-ray data confirms the orthorhombic phase of CsPbI₃ at room temperature. As obtained from bond valence calculations, strained bonds between Pb and I are identified within PbI₆ octahedral units. Morphological study shows that the as-prepared δ -CsPbI₃ forms a nanorod-like structure. The XPS analysis confirm the presence of Cs (3d, 4d), Pb (4d, 4f, 5d) and I (3p, 3d, 4d). The lithiation process involves both intercalation and conversion reactions, as confirmed by cyclic voltammetry (CV) and first-principles calculations. Impedance spectroscopy coupled with the distribution function of relaxation times identifies charge transfer processes due to Li metal foil and anode/electrolyte interfaces. An initial discharge capacity of 151 mAhg⁻¹ is found to continuously increase to reach a maximum of ~275 mAhg⁻¹ at 65 cycles, while it drops to ~240 mAhg⁻¹ at 75 cycles and then slowly decreases to 235 mAhg⁻¹ at 100 cycles. Considering the performance and structural integrity during electrochemical performance, δ -CsPbI₃ is a promising material for future Li-ion battery (LIB) application.



Citation: Kaisar, N.; Paul, T.; Chi, P.-W.; Su, Y.-H.; Singh, A.; Chu, C.-W.; Wu, M.-K.; Wu, P.M. Electrochemical Performance of Orthorhombic CsPbI₃ Perovskite in Li-Ion Batteries. *Materials* **2021**, *14*, 5718. <https://doi.org/10.3390/ma14195718>

Academic Editor: Daisuke Tashima

Received: 31 August 2021

Accepted: 28 September 2021

Published: 30 September 2021

Publisher's Note: MDPI stays neutral with regard to jurisdictional claims in published maps and institutional affiliations.



Copyright: © 2021 by the authors. Licensee MDPI, Basel, Switzerland. This article is an open access article distributed under the terms and conditions of the Creative Commons Attribution (CC BY) license (<https://creativecommons.org/licenses/by/4.0/>).

1. Introduction

Lithium-ion battery (LIB) technology is considered as the most promising energy storage technology for a wide range of applications in portable electronic devices, electric vehicles (EV) and hybrid electric vehicles (HEV) [1]. In the United States, the Department of Energy has set a cost target for EV battery packs of 125 USD/kWh to be reached in 2022, which was in large part a driving mechanism for LIB technology [2]. Given the projected policy and economic environment, and the intrinsic energy density, long cycle life and stability during long cycling, LIB was made a contending choice as a commercialized energy storage system. Negatively charged lithium anodes play an important role in maintaining the high energy density of the battery [3,4]. In spite of having extremely high theoretical specific capacity (3860 mAhg⁻¹) and low electrochemical potential (−3.04 vs. SHE), the safety risk of metallic Li hinders it from commercialization [5,6]. Commercial LIBs have graphite and lithium titanium oxide (LTO) as anode materials to achieve the market demand [7,8]. However, safety and energy density are a primary concern in those batteries. Graphite anodes face serious stability issues due to the heterogeneous dispersion of conductivity that results in the formation of imperfect solid electrolyte interphase (SEI) [9]. On the other hand, LTO exhibits outstanding stability in long-term cycling at very high C-rate while compromising safety of the battery [10]. However, low energy density and high operating voltage (1.54 vs. Li/Li⁺) made the commercialization of LTO impractical for a wide range of applications [11,12]. Recently, silicon (Si) has received

a lot of attention as a superior anode material due to its high theoretical gravimetric capacity (4200 mA h g^{-1}) and low operation voltage ($0.4 \text{ V vs. Li/Li}^+$) [13]. However, Si experiences 400% volume expansion during charge–discharge process, which affects the long cycle life due to increased probability for mechanical failure [14]. Indeed, given the environmental and material constraints, alternative anode materials for battery research should be developed to identify material choices that exhibit high energy density at low operating voltage while providing outstanding stability and safety. So far, various metal oxides, transition metal sulfides (MoS_2 , FeS_2 , Co_9S_8 , VS_2), carbon-based materials and Sn-based materials have been investigated as anode materials [15–23].

Organic and inorganic perovskites have a wide range of applications in the fields of solar cell, optoelectronics, laser and electrochromism [24–30]. Previously, scientists worked on the development of organic–inorganic perovskite materials as energy storage materials for Li-ion batteries [31–37]. However, these materials suffer from poor cycling performance and extremely low discharge capacity. The high mobility and Li^+ storage capability of hybrid perovskites inspire us to use them as active materials. Previously, the orthorhombic CsPbI_3 perovskite was successfully employed on top of Li metal to avoid the deadly dendrite, which causes failures to battery performance [38].

In this work, we report the δ - CsPbI_3 perovskite as an active anode material for Li-ion batteries. We have prepared orthorhombic CsPbI_3 by solution process at a constant temperature of 70°C . The as-prepared anode material is incorporated in a coin cell against a Li metal. Further, we have investigated the Li storage capability and structural change of host material upon lithiation by the X-ray diffraction and *ab initio* density functional theory (DFT) calculation. The active material exhibits an initial discharge capacity of 151 mAhg^{-1} upon 40 mA g^{-1} current.

2. Experimental Section

2.1. Materials Preparation

The 0.1 M CsPbI_3 solution was prepared by dissolving CsI_2 and PbI_2 (1:1) in a mixture of dimethylformamide (DMF) and dimethyl sulfoxide (DMSO) (vol 1:1) solvents. The as-prepared solution was stirred overnight at 70°C . Finally, we obtained a yellowish powder which was further grinded using mortar and pestle to achieve a fine powder.

2.2. Material Characterization

The morphology of as-prepared active material was investigated using scanning electron microscopy (SEM, JEOL-Japan, JXA-840A). To observe the changes in electrodes after cycling, the coin cells were disassembled and the electrodes were washed using 1,3-dioxolane (DOL). Later, SEM was employed to observe the change in microscopic level. The crystallinity of δ - CsPbI_3 was investigated using X-ray diffraction (XRD) technique using Philips X'Pert diffractometer equipped with a $\text{Cu K}\alpha$ X-ray source ($\lambda = 1.5406 \text{ \AA}$) in the 2θ range of 10° – 50° . A JacobsV-670 UV–Vis spectrometer was employed to confirm the presence of absorption peaks of the δ - CsPbI_3 and the band gap was calculated the Tauc plot. XPS (PHI 5000 Versa Probe and an $\text{Al K}\alpha$ X-ray source = 1486.6 eV) was employed to study the binding energy of central metal ion Pb of δ - CsPbI_3 . Coin cells were assembled using δ - CsPbI_3 electrode and after first discharge, the cell was opened and the electrode was washed with DOL and dried prior to transfer inside the XPS chamber.

2.3. Electrochemical Measurement

δ - CsPbI_3 loaded electrodes were prepared by mixing 65% δ - CsPbI_3 with 20% carbon black and 15% poly (vinylidene fluoride) (PVDF) binder. The powders were mixed in *N*-methyl-2-pyrrolidinone (NMP) solvent. As-obtained slurry was coated on Cu foil and dried overnight at 50°C . Later, the electrode was cut into a 12 mm disk in order to prepare the coin cells. A 12 mm Li disk was used as the counter electrode. Electrolyte 1 M LiPF_6 was prepared by mixing ethylene carbonate (EC) and dimethyl carbonate (DMC) (1:1 vol). A pristine Celgard separator was used in between two electrodes for safety reasons. CR2032-

type coin cells were assembled in an Ar-filled glove box. Galvanostatic charge–discharge of the coin cells was performed using Think Power battery testing system. PARSTAT MC 1000 electrochemistry workstation was employed to measure the cyclic voltammetry (CV) and electrochemical impedance spectroscopy (EIS). CV tests were performed on the cells in a voltage window of 0.1–3 V and at a scan rate of 0.1 mV s^{−1}. EIS of the cells were performed with an AC amplitude of 10 mV and the frequency range was from 0.01 Hz to 1 MHz.

2.4. Theoretical Treatment

The distribution function of relaxation times (DFRTs) was calculated by the Impedance Spectroscopy Genetic Programming (ISGP) program using the impedance spectra after different cycles [39–44]. As the DFRT approach is applicable only in the Kramers–Krönig (KK) relations compatible regime, the supporting figure (Supplementary Materials, Figure S19) suggests that we can safely identify three peaks within the KK compatible regime (around 0.1 Hz). A similar approach is also adopted elsewhere [39–41,45]. The Rietveld refinement of the XRD pattern was performed by FullProf software package, the Fourier maps were calculated using GFourier and the crystal structure was plotted using VESTA [46,47].

The electronic structure calculation was performed using the Quantum ESPRESSO (QE) distribution, based on density-functional theory, periodic boundary conditions, plane-wave basis sets and pseudopotentials [48,49]. The GBRV ultrasoft pseudopotentials at a plane-wave cutoff of 40 Ry and a charge-density cutoff of 200 Ry were selected for all the calculations with a Gamma-centered k-point mesh [50]. The structure optimization was carried out using a conjugate-gradient algorithm until the forces on each atom were less than 0.01 eV Å^{−1} and the total energy was converged up to 10^{−5} eV. To study the lithium intercalated structures of 0.5, 1, 2, 3 and 4, supercells of LiCs₈Pb₈I₂₄, LiCs₄Pb₄I₁₂, Li₂Cs₄Pb₄I₁₂, Li₄Cs₄Pb₄I₁₂ and Li₈Cs₄Pb₄O₁₂ structures with their stable configuration have been considered, respectively.

3. Results and Discussion

1 M δ-CsPbI₃ was prepared by mixing CsI₂ and PbI₂ in DMF and DMSO solvent which results in a yellow solution (Figure S1a). The mixture was stirred overnight inside a N₂ filled glove box at 70 °C. We received a yellowish CsPbI₃ powder as our final active material (Figure S1b). Figure 1 exhibits the crystal structure of δ-CsPbI₃ and diffraction peaks assigned to orthorhombic structure or δ-phase as determined by the Rietveld refinement [51]. Although most of the perovskites are air-sensitive, δ-CsPbI₃ is extremely stable in air [52]. δ-CsPbI₃ maintains its crystallinity as confirmed by the present solution method. According to previous reports, CsPbI₃ exists in four crystal phases: α, β, γ and δ [53]. Out of all the studied phases, the δ phase is stable in air, and an orthorhombic structure gives sufficient space for Li intercalation–deintercalation [52]. The diffraction pattern of the δ-CsPbI₃ at room temperature has been indexed with orthorhombic phase (space group Pnma) having lattice parameters $a = 10.4595(3)$ Å, $b = 4.8034(15)$ Å and $c = 17.7754(4)$ Å, $\alpha = \beta = \gamma = 90^\circ$ with a cell volume of 893.055 Å³ which is in accordance with ICSD File #250744. The convergence of the refinement is achieved with the residuals of $R_B = 7.87\%$, $R_F = 5.75\%$ and $\chi^2 = 7.34$, and the refined structural parameters are shown in Table 1. The XRD patterns at different lithiation potentials, determined by CV measurement shown in Figure S2, have a smaller number of peaks in comparison with the pristine powder. Preferred orientation of the Bragg peaks in 2θ around 43° and 50° (Figure S2), and Figure S3 (red curve), supports the conversion reactions. For instance, the peaks at 42.93°, 50.07°, 27.23° in panel (b), and 42.95°, 50.10° in panel (c) can be attributed to δ-CsPbI₃; 25.88°, 31.06° are associated with PbI₂ and 36.02°, 52.02° in panel (d) are from PbLi, as confirmed from ICSD Files #250744, #104762, #68819, #24265, respectively. This suggests the coexistence of both pristine and conversion reacted phases at different potentials. The Rietveld refinements of the XRD patterns for both pristine and after 100 cycles (Figure S4 with orthorhombic phase) suggest an increase in unit cell volume (896.747–893.055 = 3.692 Å³) indicating lithiation in the cell as well as shallow charging/discharging processes. Furthermore, the lithiation

potential calculation by DFT supports this conjecture (see later section). However, the pristine structure changes due to prolonged cycling as well as reaction times of lithiation (Figures S2 and S3). Additionally, the presence of Li_xPF_y moieties as confirmed by the XPS studies further justifies the lithiation process (see Figures S12 and S13, and Equation (1)).

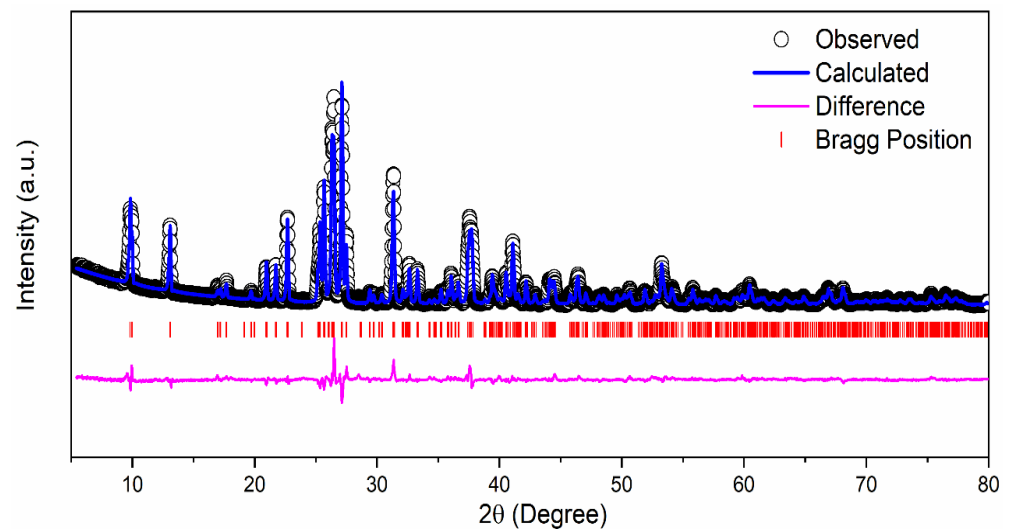


Figure 1. Rietveld refinement of the XRD pattern of $\delta\text{-CsPbI}_3$ at room temperature.

Table 1. At room temperature.

| Label of Atom | Atom | Wyckoff Site | Atomic Coordinates | | | Occupancy |
|---------------|------|--------------|--------------------|--------|---------|-----------|
| | | | x | y | z | |
| Pb | Pb | 4c | 0.16099 | 0.2500 | 0.43864 | 1 |
| I1 | I | 4c | 0.16396 | 0.2500 | 0.00343 | 0.995 |
| I2 | I | 4c | 0.29759 | 0.2500 | 0.28639 | 0.974 |
| I3 | I | 4c | 0.03533 | 0.2500 | 0.61563 | 1 |
| Cs | Cs | 4c | 0.41541 | 0.2500 | 0.66999 | 1 |

The perovskite structure of $\delta\text{-CsPbI}_3$ has distorted PbI_6 octahedral with a distortion index of 0.025 \AA and two Pb-I1, three Pb-I3 and single Pb-I2 distances of $3.232(7) \text{ \AA}$, $3.303(7) \text{ \AA}$, $3.409(7) \text{ \AA}$ and $3.060(6) \text{ \AA}$, respectively (Figure S5). The average I-I distances are calculated as $4.188(9) \text{ \AA}$ to $4.803(15) \text{ \AA}$. In this context, the electron density distributions along (110) plane are calculated to find any discrepancy between the observed and calculated structure factors. As observed from Figures S6 and S7, the positive electron densities at two highly localized I1 sites justify the proper fitting of the model. Nevertheless, the contour lines suggest the ionic bonding between I sites. The bond-valence parameters have been calculated using the Zachariasen formula to be 1.923 v.u., 1.029 v.u., 1.081 v.u., 0.928 v.u. and 1.106 v.u. for Pb, I1, I2, I3 and Cs sites, respectively. Interestingly, the variation in the bond-valence parameter of I changes due to different atomic coordinates and occupancies (see Table 1). These deviations from their original valence states indicate the strained bonding inside the polyhedral units, and these have a direct effect on battery performance as observed here and elsewhere [54].

Anisotropic thermal factors for the same elements are shown below (Table 2).

Table 2. Anisotropic thermal factors for the same elements.

| Label of Atom | B ₁₁ | B ₂₂ | B ₃₃ | B ₁₂ | B ₁₃ | B ₂₃ |
|---------------|-----------------|-----------------|-----------------|-----------------|-----------------|-----------------|
| Pb | 0.00148 | 0.04421 | 0.00015 | 0 | 0.00088 | 0 |
| I1 | 0.00302 | 0.01320 | 0.00154 | 0 | 0.00173 | 0 |
| I2 | −0.00049 | 0.05040 | 0.00014 | 0 | 0.00023 | 0 |
| I3 | 0.00127 | 0.04586 | 0.00086 | 0 | −0.00028 | 0 |
| Cs | −0.00077 | 0.07601 | 0.00194 | 0 | 0.00076 | 0 |

Figure 2a,b shows regular and uniform nanorod-like structures with an average length of 5–7 μm and diameter of ~ 400 nm of $\delta\text{-CsPbI}_3$. The average particle size is 5.5 μm which is calculated from particle size distribution histogram (Figure S8). An absorption peak is observed between 425–450 nm when UV-vis spectra was collected for $\delta\text{-CsPbI}_3$ (Figure S9). Tauc plot shows a band gap of 2.644 eV as obtained from the optical absorption spectrum. DFT-based density of states (DOS) is used to investigate how the lithium ion affects the electronic structure of the $\delta\text{-CsPbI}_3$ perovskite. From Figure S10, $\delta\text{-CsPbI}_3$ shows a band gap of 2.132 eV similar to that obtained for CsPbBr_3 [55]. Our results suggest that Perdew–Burke–Ernzerhof (PBE) underestimates the experimental band gap up to 21%. The top-view SEM image (Figure 2c) shows that the CsPbI_3 is uniformly distributed. Figure 2d shows ~ 15 μm electrode coated on the Cu foil. An XPS survey spectrum is performed to confirm the compositions of CsPbI_3 , Cs, Pb and I_2 at their corresponding binding energies (Figure 2e).

The impedance measurements were carried out in the pristine cell as well as after several charge–discharge cycles (Figure 3a). We have also plotted the impedance data for a $\text{Li}|\text{Li}$ symmetric cell for comparison. It is observed that the overall impedance response contains a single semicircular arc with spike-like extensions at low frequencies. With increasing charge–discharge cycles, the diameter of the semicircular arc decreases and shows an abrupt change after maximum 60 cycling. To understand the electrochemical phenomenon qualitatively, the impedance data have been modeled by ISGP, neglecting the capacitive diffusive regime at low frequencies. The program computes the distribution function of relaxation times which comprises several peaks justifying some electrochemical phenomena. As observed from Figure 3b, the Distribution Function Relaxation Times (DFRTs) for all the conditions show three peaks within the experimental frequency range. A tiny peak at the highest frequencies corresponds to the Ohmic drop due to electrolytic resistances (Peak P1). The peak within the 10^2 to 10^4 Hz regime corresponds to lithium metal, which is related to the charge transfer processes along the metal surface (Peak P2) [56,57]. The peak shifts towards low frequencies with initial cycling but vanishes after 100 cycles, indicating loss of the reactivity of the lithium metal. Additionally, the charge transfer resistance decreases with increasing cycles, justifying good electronic transport (Figure S11). At pristine condition, due to the initial SEI layer at anode, lithium activity maintains an equilibrium which dilutes with increasing cycle numbers and as a result, the resistance decreases. Secondly, the peak within $10\text{--}10^{-2}$ Hz corresponds to the charge transfer of lithium ions at the anode/electrolyte interface and exhibits strong frequency dependence (Peak P3) [56]. This charge transfer process becomes slower with increasing cycle numbers. A close inspection shows that the peak P3 for cycles 2 and 3, unlike cycles 1 and 70 (Figure 3a inset), has broader time distribution which is due to small variation in their impedance plots. It seems that the charge transfer processes are important in explaining the state-of-health of the batteries and can be used as representative fingerprinting for such high-capacity behavior.

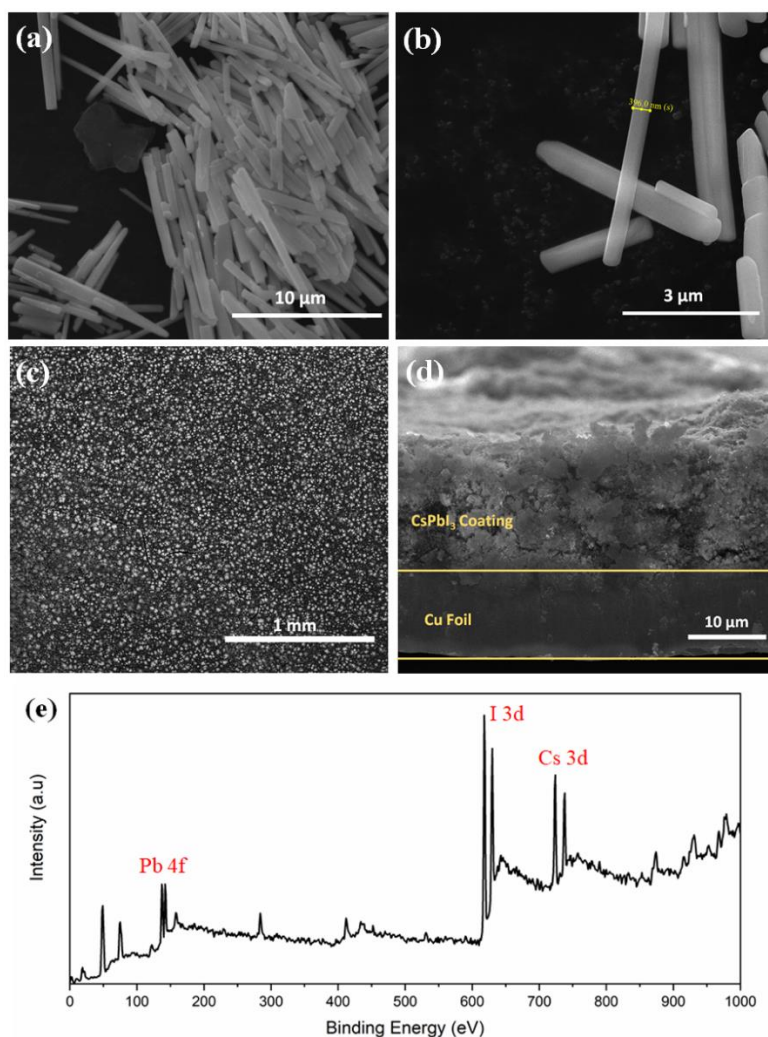


Figure 2. Morphology analysis. (a,b) FESEM image of as-prepared δ -CsPbI₃ using solution process at different magnifications. (c) Top view FESEM image of electrode using δ -CsPbI₃ and PVDF, carbon black pasted on Cu foil. (d) Cross-sectional FESEM image of as prepared electrode on Cu foil. (e) XPS survey spectrum of δ -CsPbI₃ as prepared by solution process.

The XPS spectra in Figure 4a reveal the electrochemical interaction of lithium with δ -CsPbI₃. Both spectra contain peaks from Cs (3d, 4d), Pb (4d, 4f, 5d) and I (3p, 3d, 4d) and with a decrease in their intensities (except O and F) in the material after charging–discharging cycle, suggesting a coating of surface film on the active electrode [58,59]. A tiny peak at 532 eV of O 1s is observed which could be due to Li alkoxy species: CH₃OLi (from reduction of DMC) and (CH₂OLi)₂ (from reduction of EC) compounds as obtained (Figure 4a) [60]. Secondly, the peak becomes sharper after the discharging condition. A peak at 286 eV corresponds to unavoidable C 1s peak (C-C). XPS spectra exhibit the Pb²⁺ states and the binding energies 138.8 and 143.7 eV, corresponding to 4f_{7/2} and 4f_{5/2}, respectively (Figure 4b). Previously, it was reported that due to the influence of external ions/factors, there might be change in oxidation state of Pb²⁺ or redistribution of electron charges around Pb²⁺ [55,61]. The binding energies shifted from 138.8 to 137.7 eV and 143.7 to 142.77 eV, respectively. The absence of I 4d_{5/2} peak at 49 eV and I 3d_{5/2} and 3d_{3/2} around 630 eV confirm that the discharging effect is associated with iodine. Overall, as obtained from the XRD refinement results, the PbI₆ octahedra are associated with the lithiation process. As expected, no LiF peaks are detected in the pristine electrode. Another important feature is that the F 1s spectra at 688 eV was observed after discharged

(Figure S12). The F 1s spectra consists of two peaks around 685 eV (due to LiF) and 687 eV due to Li_xPF_y with the following reduction reactions [60]:

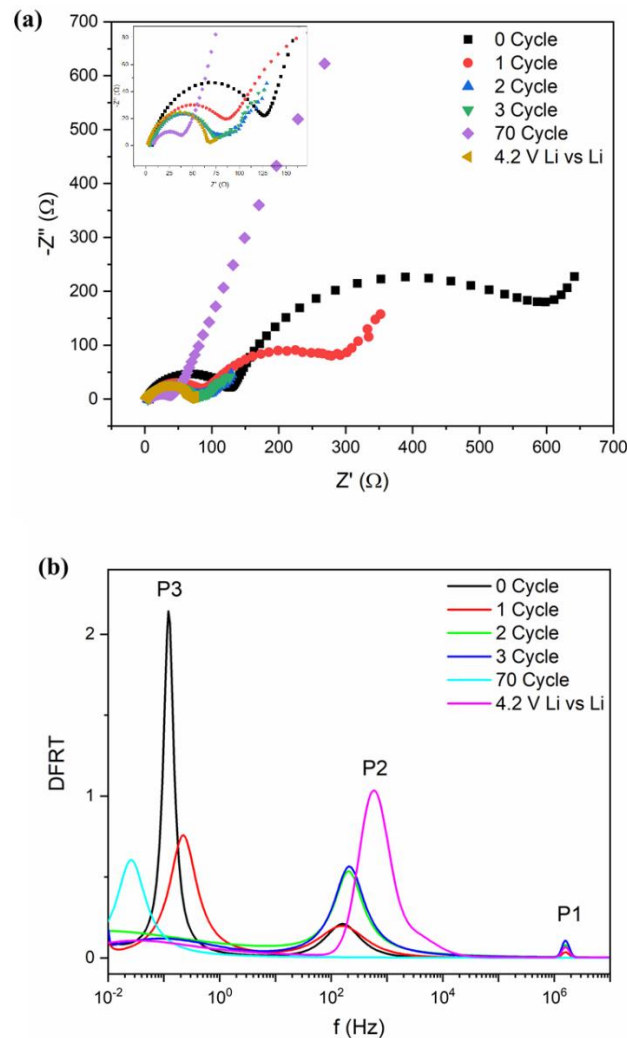
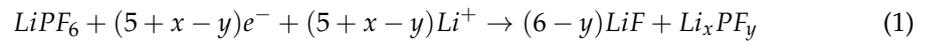


Figure 3. (a) Nyquist plots of impedance after different cycles along with symmetric Li cell. (b) DFRTs for Li-ion batteries after different cycling measurements. Inset of (a): zoom-in figure of impedance.

The Li 1s peak at 56 eV can be observed (LiF) (Figure S13) and the P 2p peak (138 eV) is masked with Pb 4f, inferring Li_xPF_y moieties. On the other hand, a relatively higher O 1s peak suggests $\text{Li}_x\text{PF}_y\text{O}_z$ moieties. Since the electrode is washed thoroughly with DMC before the measurements, the peaks relating to F 1s and P 2p may not be due to original LiPF_6 . Thus, the surface of the electrode is modified by different species such as LiF, Li_xPF_y and $\text{Li}_x\text{PF}_y\text{O}_z$ due to the first discharged cycle.

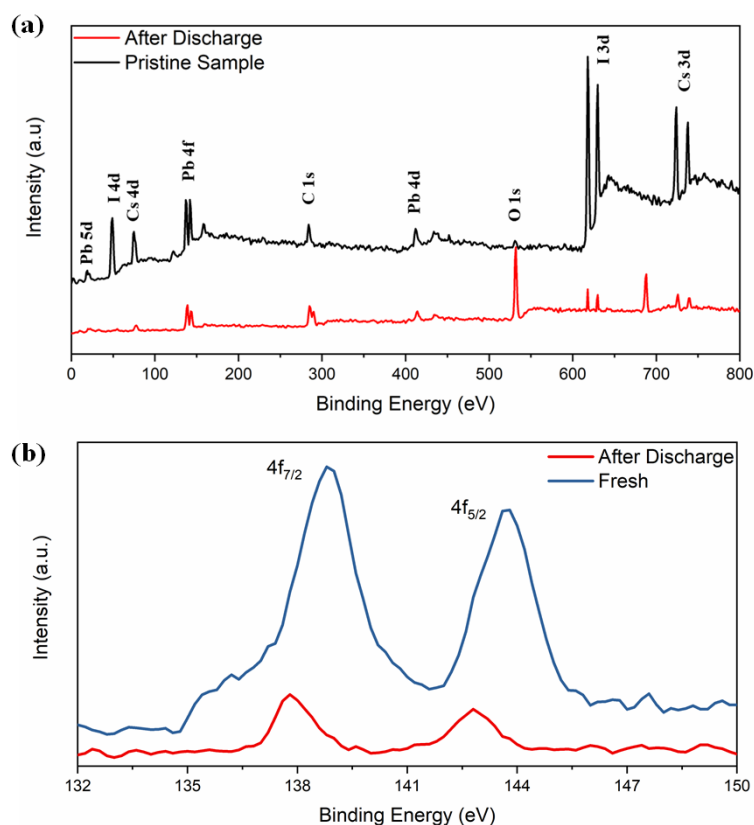


Figure 4. (a) Full scan XPS spectra of CsPbI₃, (b) XPS spectra of Pb 4f before and after electrochemical discharging process.

Figure 5a represents the cyclic voltammetry (CV) of Li-ion coin cells with δ -CsPbI₃ as anode materials. The CV is performed within a voltage range of 0.1–3 V at a scan rate of 0.1 mV s⁻¹. During delithiation, two peaks at 0.58 V and 0.7 V vs. Li/Li⁺ are noted, which have been reported for MAPbBr₃ [62]. Furthermore, during lithiation, the peaks between 0.4–0.6 V can be attributed to Li_xPb such as LiPb and Li_{2.6}Pb as identified previously for PbO₂, PbO and Pb electrodes [63]. It is noted that similar characteristic features of alloying and dealloying have been reported for 2D and 3D hybrid perovskites [64]. Structural defragments due to alloying are also noted from SEM images (Figures S14 and S15). Concerning the peak positions and their variations in CV and XPS spectra, the following electrochemical reaction is proposed: CsPbI₃ + Li⁺ + e⁻ → Li_xCsPbI₃ (during discharging). Theoretically, to determine the lithiation potential in CsPbI₃, Li-ion is considered to be inserted in the primitive orthorhombic unit cell of CsPbI₃ (20 atoms) with its different stoichiometries. Since in the pristine structure, Cs, Pb and I-ions occupy 4c sites, we have chosen 8d, 4c, 4b and 4a as interstitial lithiation sites. The geometry optimization calculations suggest that the ground state configuration energy is the same for all the sites with the same Li atoms per unit cell (as listed in Table S1). Based on the CV curve (Figure 5a), the peaks between 0.4 V–0.6 V can be associated with Li_xPb such as LiPb, Li_{2.6}Pb as previously observed for Pb-, PbO₂- and PbO-based electrodes, whereas the peak around 1.4 V is due to Li_xCsPbI₃ (Figure 6a). To identify the quantity of the intercalated lithium ion per unit cell, we have performed geometry optimization in QE with x = 0.5, 1, 2, 3 and 4 Li-ions only at 8d site of the host structure. Figure 6a shows a difference in the insertion voltages at each x referring to a single-phase and one step mechanism of lithiation, and a variation in the lattice parameters is observed (Figure 6b). For instance, the lithiation reaction having 0.5 Li-ion will be CsPbI₃ + 0.5Li⁺ + e⁻ → Li_{0.5}CsPbI₃. Nevertheless, the simulated XRD patterns of Li_{0.5}CsPbI₃, LiCsPbI₃, Li₂CsPbI₃, Li₃CsPbI₃ and Li₄CsPbI₃ are similar to that of the pristine structure (orthorhombic phase). Indeed, the parent structure is an indirect band gap semiconductor, but with an insertion of 0.5 Li per unit

cell, the structure becomes semi-metallic (Figure S10). However, the band gap widens with an increase of lithium content (Figure S16). The formation energy and the average Li intercalation potential curves in Figure 6 show that with increasing lithiation, the magnitude of the formation energy increases and the average Li intercalation potential decreases. As the formation energy of lithiation is less than 0 eV, the intercalation is definitely possible. However, the discharge curve in CV suggests that conversion reaction relating Li_xPb starts around 0.6 V (Figure 5a). Thus, we can confirm that both intercalation and conversion have occurred during the whole discharge process, and due to the conversion process, a structural phase transition may exist (Figures S2 and S3). Comparing Figure 5a,b and Figure 6, the kinks in the discharge CV curve around 1.4 V and 1.0 V can be attributed to $\text{Li}_{0.5}\text{CsPbI}_3$ and $\text{Li}_4\text{CsPbI}_3$, respectively. It is noted that similar insertion and conversion reactions during discharging are reported for the $\text{W}_{18}\text{O}_{49}$ anode [65,66]. Nevertheless, the unit cell volume expands for the lithiated structures (Figure 6b). It is observed that a small volume change is a direct consequence of the low-density perovskite structure of allotrope CsPbI_3 , facilitating Li-ion movement with minimal lattice distortion. The CV results indicate that the electrochemical reduction of $\delta\text{-CsPbI}_3$ is reversible. Additionally, the peaks at charging condition do not show any voltage drift, signifying a steady formation of SEI layer as well as no electrolyte oxidation during the cell operation [67]. Figure 5b exhibits dQ/dV profiles ranging from 0.01 to 3 V without any loss of capacitance during the first cycle. This feature establishes its applicability as an anode material in comparison with graphite [68]. The post-cycling cell (after 100 charge–discharge cycles) was tested in similar condition, in order to observe the impact of lithiation/delithiation on the CV of the active material. Figure S17 shows the reversible CV profile of $\delta\text{-CsPbI}_3$ after 100 cycles inferring negligible loss of active material during long cycling, and as a result, the capacity is maintained around the same as that after 75 cycles. The SEM image of $\delta\text{-CsPbI}_3$ electrode after 100 cycles observed shows a smooth and integrated surface (Figure S14). Figure S15 is the cross-sectional image of the electrode after 100 charge–discharge cycles showing the coating remains intact with the Cu foil. This study suggests that the $\delta\text{-CsPbI}_3$ electrode has good integrity throughout a long cycle life and that there is no loss of active materials during cycling. Later, we disassembled the cell and washed and dried the electrode to observe the XRD peak. Figure S4 shows major peaks for $\delta\text{-CsPbI}_3$ maintained after 100 cycles.

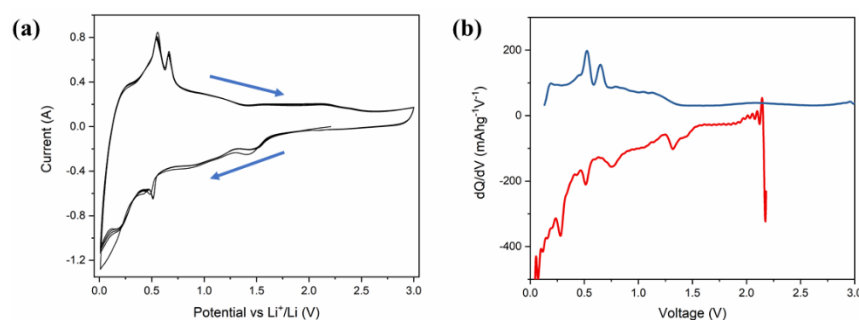


Figure 5. Electrochemical performance of $\delta\text{-CsPbI}_3$ active materials in Li-ion half-cell. (a) Cyclic voltammetry trace of a $\delta\text{-CsPbI}_3$ half-cell within a voltage window of 0.1–3.0 V, recorded at a scan rate of 0.1 mV s^{-1} . (b) Incremental capacity dQ/dV vs. cell potential as recorded at a rate of 40 mA g^{-1} for first electrochemical cycle.

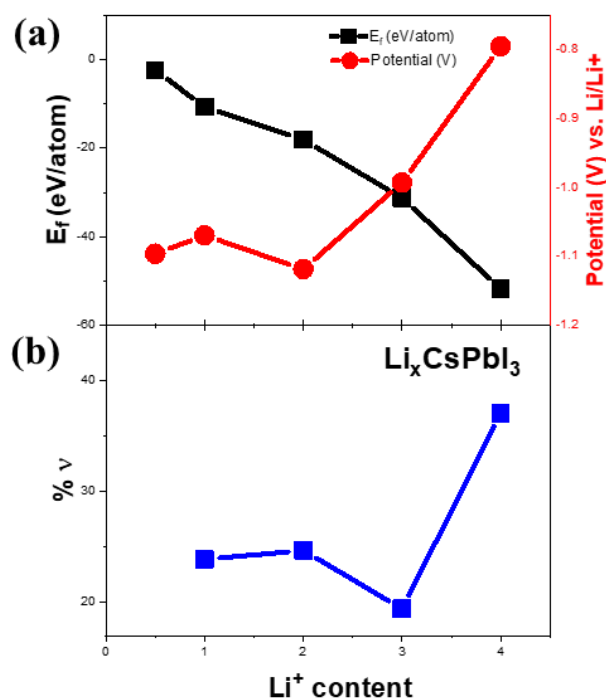


Figure 6. (a) Calculation of formation energies as a function of lithium content. The right vertical axis represents the lithiation potential as a function of lithium content in (a). Theoretically calculated volume change (%v) as a function of lithium content is shown in (b).

Figure 7 exhibits the long-term cycling performance of Li-ion battery using δ -CsPbI₃ as active material at 40 mA g⁻¹. The δ -CsPbI₃ electrode suffers from a capacity drop in the first six charge–discharge cycles from 151 mAhg⁻¹ to 149.8 mAhg⁻¹. From seventh cycle, the capacity started to increase steadily with an increase rate of 2.12 mAhg⁻¹ per cycle to reach a maximum of ~275 mAhg⁻¹ at 65 cycles. After that, it drops to ~240 mAhg⁻¹ at 75 cycles and then slowly decreases to 235 mAhg⁻¹ at 100 cycles. This phenomenon suggests that Li-ion accessibility increases inside the active material along with oxygen containing functional groups with increasing the cycling number. This can be observed in Figure S9 with reversible CV of active material after 70 cycles. Additionally, this could be due to a large surface area (SEM) and high oxygen adsorption at the surface as supported by the XPS spectrum (Figure 4a). There are a few valid reasons behind a slight increase in discharge capacity which are as follows: (a) due to increase in activation of the active materials, (b) activation of defects in the active materials, and (c) enlargement of active materials' interatomic space after a few charge–discharge cycles (as understood from increment from lattice parameters) [69–71]. Another possibility is that there is a conversion reaction happening at low voltages which could suppress the intercalation, and due to the conversion reaction, the structural defragment is obtained (Figure S2). Overall, the capacity has increased Li-ion accessibility inside the active material along with oxygen containing functional groups with an increase in the cycling number. The Coulombic efficiency was maintained throughout the cycling performance, which suggests a reversibility of Li insertion/disinsertion during electrochemical process. This cycling performance reveals that Li⁺ can intercalate–deintercalate during the charge–discharge process, and it is a reversible process [72,73]. This suggests the Li⁺-ion movement during cycling was smooth and avoided thicker SEI formation [74]. Furthermore, as suggested by the dQ/dV plot (Figure 5b), there is a negligible SEI layer in comparison with that of graphite [74].

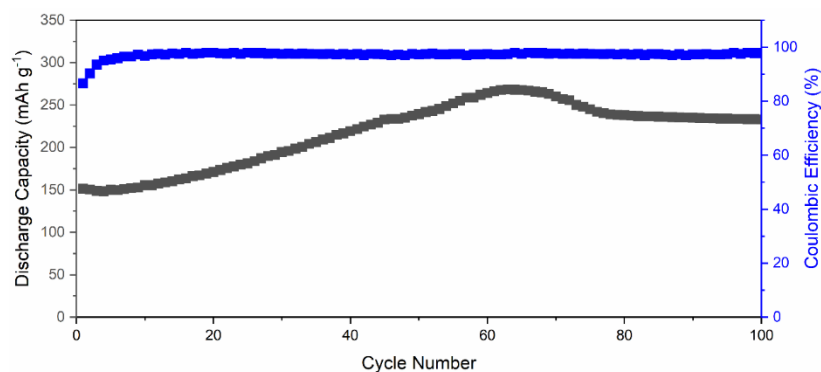


Figure 7. Long-term cycling performance of a Li-ion battery featuring δ -CsPbI₃ as active materials, tested at 0.1C-rate.

We have shown the cycling performance at different C-rates to evaluate the cycling stability of the active material. As displayed in Figure S18, the cell exhibits an initial discharge capacity of 181 mAhg⁻¹ when discharged at 0.1 C-rate. After tested through harsh charge–discharge conditions at different C-rates, the cell retains ~84% of the initial discharge capacity, which shows outstanding cycling performance of the CsPbI₃ as an active anode material.

4. Conclusions

We have successfully introduced δ -CsPbI₃ as an active anode material for Li-ion battery. The perovskite structure of δ -CsPbI₃ has distorted PbI₆ octahedra as calculated by the X-ray refinement. Ionic bonding between I sites are observed along with a partial vacancy up to 0.03%. We propose that the presence of the functional species has a beneficial effect in terms of discharge capacity. Specifically, the charge transfer processes along the Li metal surface and that at the anode/electrolyte interface are identified, and both of them show constant frequency shifts with increasing cycling. We conclude that both intercalation and conversion have occurred during the whole discharge process using ex situ XRD, CV and first-principles calculations. The electrochemical performance of δ -CsPbI₃ shows outstanding potential as a promising anode material for commercialized Li-ion batteries. We need more extensive studies to stabilize performance while at the same time increasing their capacity.

Supplementary Materials: The following are available online at <https://www.mdpi.com/article/10.3390/ma14195718/s1>, Figure S1: (a) Photograph of δ -CsPbI₃ solution during preparation, and (b) as-prepared δ -CsPbI₃ powder; Figure S2: XRD of fresh CsPbI₃ and after one cycle at various voltages during discharging; Figure S3: XRD patterns of pristine CsPbI₃, CsPbI₃ with LiPF₆ salt and CsPbI₃ after dipping in electrolyte for different time along with Li metal foil at room temperature; Figure S4: Rietveld refinement of the XRD pattern of δ -CsPbI₃ after 100 cycles at room temperature; Figure S5: Orthorhombic structure of δ -CsPbI₃. PbI₆ octahedral units are shown in gray color; Figure S6: Electron density distribution of observed structure factors along (110) plane of δ -CsPbI₃; Figure S7: Electron density distribution of calculated structure factors along (110) plane of δ -CsPbI₃; Figure S8: Particle size distribution for CsPbI₃ from SEM image; Figure S9: Optical absorption spectra of CsPbI₃ collected by dissolving as-prepared CsPbI₃ powder in DMF solvent. (a) UV-Vis spectra and (b) Tauc plot; Figure S10: Total DOS for CsPbI₃ and LiCsPbI₃. The vertical line represents Fermi level: EF; Figure S11: Variation of the charge transfer resistances along the metal surface with cycles; Figure S12: XPS spectra of F 1s before and after electrochemical discharging process; Figure S13: XPS spectra of Li 1s after electrochemical discharging process; Figure S14: Top view FESEM image of δ -CsPbI₃ electrode after 100 charge-discharge cycles at 40 mA g⁻¹. Figure S15: Cross sectional FESEM image of δ -CsPbI₃ electrode after 100 charge-discharge cycles at 40 mA g⁻¹; Figure S16: Total DOS for several lithiated compounds along with pristine CsPbI₃. The vertical line represents Fermi level: EF; Figure S17: Cyclic voltammetry trace of a δ -CsPbI₃ half-cell after 100 Charge-discharge

cycles within a voltage window of 0.1–3.0 V, recorded at a scan rate of 0.01 mV s⁻¹.; Figure S18: Cycling performance of CsPbI₃ anode materials at different C-rate.; Figure S19: KK compatibility test.; Table S1: Ground state energy for different configuration of lattice sites with different concentration of lithiation.

Author Contributions: Data curation, N.K., P.-W.C. and Y.-H.S.; formal analysis, N.K., T.P. and P.-W.C.; funding acquisition, M.-K.W.; investigation, M.-K.W. and P.M.W.; methodology, N.K., P.-W.C., Y.-H.S. and A.S.; project administration, M.-K.W. and P.M.W.; resources, M.-K.W.; software, T.P.; supervision, C.-W.C., M.-K.W. and P.M.W.; writing—original draft, N.K.; writing—review & editing, N.K., T.P., M.-K.W. and P.M.W. All authors have read and agreed to the published version of the manuscript.

Funding: The authors greatly appreciate the financial supports from the Executive Yuan through its Forward-Looking Research Grant Number 110-0210-04-20-01. Dr. Phillip M. Wu acknowledges the support of visiting scholar program under Grant Number 109-2811-E-027-506 from the Ministry of Science and Technology (MOST) of Taiwan.

Institutional Review Board Statement: Not applicable.

Informed Consent Statement: Not applicable.

Data Availability Statement: The data presented in this study are available on request from the corresponding author.

Conflicts of Interest: The authors declare no conflict of interest.

References

1. Dunn, B.; Kamath, H.; Tarascon, J.-M. Electrical Energy Storage for the Grid: A Battery of Choices. *Science* **2011**, *334*, 928–935. [[CrossRef](#)] [[PubMed](#)]
2. Chu, S.; Cui, Y.; Liu, N. The Path Towards Sustainable Energy. *Nat. Mater.* **2017**, *16*, 16–22. [[CrossRef](#)] [[PubMed](#)]
3. Liu, D.-H.; Bai, Z.; Li, M.; Yu, A.; Luo, D.; Liu, W.; Yang, L.; Lu, J.; Amine, K.; Chen, Z. Developing High Safety Li-Metal Anodes for Future High-Energy Li-Metal Batteries: Strategies and Perspectives. *Chem. Soc. Rev.* **2020**, *49*, 5407–5445. [[CrossRef](#)]
4. Shen, X.; Li, Y.; Qian, T.; Liu, J.; Zhou, J.; Yan, C.; Goodenough, J.B. Lithium Anode Stable in Air for Low-Cost Fabrication of a Dendrite-Free Lithium Battery. *Nat. Commun.* **2019**, *10*, 900. [[CrossRef](#)] [[PubMed](#)]
5. Xu, W.; Wang, J.; Ding, F.; Chen, X.; Nasybulin, E.; Zhang, Y.; Zhang, J.-G. Lithium Metal Anodes for Rechargeable Batteries. *Energy Environ. Sci.* **2014**, *7*, 513–537. [[CrossRef](#)]
6. Dai, H.; Gu, X.; Dong, J.; Wang, C.; Lai, C.; Sun, S. Stabilizing Lithium Metal Anode by Octaphenyl Polyoxyethylene-Lithium Complexation. *Nat. Commun.* **2020**, *11*, 643. [[CrossRef](#)] [[PubMed](#)]
7. Chen, K.-H.; Namkoong, M.J.; Goel, V.; Yang, C.; Kazemiabnavi, S.; Mortuza, S.; Kazyak, E.; Mazumder, J.; Thornton, K.; Sakamoto, J. Efficient Fast-Charging of Lithium-Ion Batteries Enabled by Laser-Patterned Three-Dimensional Graphite Anode Architectures. *J. Power Sources* **2020**, *471*, 228475. [[CrossRef](#)]
8. Odziomek, M.; Chaput, F.; Rutkowska, A.; Świerczek, K.; Olszewska, D.; Sitarz, M.; Lerouge, F.; Parola, S. Hierarchically Structured Lithium Titanate for Ultrafast Charging in Long-Life High Capacity Batteries. *Nat. Commun.* **2017**, *8*, 15636. [[CrossRef](#)] [[PubMed](#)]
9. Fu, L.; Endo, K.; Sekine, K.; Takamura, T.; Wu, Y.; Wu, H. Studies on Capacity Fading Mechanism of Graphite Anode for Li-Ion Battery. *J. Power Sources* **2006**, *162*, 663–666. [[CrossRef](#)]
10. Amine, K.; Belharouak, I.; Chen, Z.; Tran, T.; Yumoto, H.; Ota, N.; Myung, S.T.; Sun, Y.K. Nanostructured Anode Material for High-Power Battery System in Electric Vehicles. *Adv. Mater.* **2010**, *22*, 3052–3057. [[CrossRef](#)]
11. Yi, T.-F.; Liu, H.; Zhu, Y.-R.; Jiang, L.-J.; Xie, Y.; Zhu, R.-S. Improving the High Rate Performance of Li₄Ti₅O₁₂ through Divalent Zinc Substitution. *J. Power Sources* **2012**, *215*, 258–265. [[CrossRef](#)]
12. Xue, X.; Yan, H.; Fu, Y. Preparation of Pure and Metal-Doped Li₄Ti₅O₁₂ Composites and Their Lithium-Storage Performances for Lithium-Ion Batteries. *Solid State Ion.* **2019**, *335*, 1–6. [[CrossRef](#)]
13. Cho, J. Porous Si Anode Materials for Lithium Rechargeable Batteries. *J. Mater. Chem.* **2010**, *20*, 4009–4014. [[CrossRef](#)]
14. McDowell, M.T.; Lee, S.W.; Wang, C.; Cui, Y. The Effect of Metallic Coatings and Crystallinity on the Volume Expansion of Silicon During Electrochemical Lithiation/Delithiation. *Nano Energy* **2012**, *1*, 401–410. [[CrossRef](#)]
15. Hassan, M.F.; Guo, Z.; Chen, Z.; Liu, H.-K. Carbon-Coated Moo₃ Nanobelts as Anode Materials for Lithium-Ion Batteries. *J. Power Sources* **2010**, *195*, 2372–2376. [[CrossRef](#)]
16. Qiao, H.; Xiao, L.; Zhang, L. Phosphatization: A Promising Approach to Enhance the Performance of Mesoporous TiO₂ Anode for Lithium Ion Batteries. *Electrochem. Commun.* **2008**, *10*, 616–620. [[CrossRef](#)]
17. Kashale, A.A.; Ghule, K.A.; Gattu, K.P.; Ingole, V.H.; Dhanayat, S.S.; Sharma, R.; Ling, Y.-C.; Chang, J.-Y.; Vadiyar, M.M.; Ghule, A.V. Annealing Atmosphere Dependant Properties of Biosynthesized TiO₂ Anode for Lithium Ion Battery Application. *J. Mater. Sci. Mater. Electron.* **2017**, *28*, 1472–1479. [[CrossRef](#)]

18. Hwang, H.; Kim, H.; Cho, J. MoS₂ Nanoplates Consisting of Disordered Graphene-Like Layers for High Rate Lithium Battery Anode Materials. *Nano Lett.* **2011**, *11*, 4826–4830. [[CrossRef](#)] [[PubMed](#)]
19. Zhang, D.; Mai, Y.; Xiang, J.; Xia, X.; Qiao, Y.; Tu, J. FeS₂/C Composite as an Anode for Lithium Ion Batteries with Enhanced Reversible Capacity. *J. Power Sources* **2012**, *217*, 229–235. [[CrossRef](#)]
20. Zhou, Y.; Yan, D.; Xu, H.; Feng, J.; Jiang, X.; Yue, J.; Yang, J.; Qian, Y. Hollow Nanospheres of Mesoporous Co₉S₈ as a High-Capacity and Long-Life Anode for Advanced Lithium Ion Batteries. *Nano Energy* **2015**, *12*, 528–537. [[CrossRef](#)]
21. Jing, Y.; Zhou, Z.; Cabrera, C.R.; Chen, Z. Metallic V_s2 Monolayer: A Promising 2d Anode Material for Lithium Ion Batteries. *J. Phys. Chem. C* **2013**, *117*, 25409–25413. [[CrossRef](#)]
22. Ming, F.; Liang, H.; Lei, Y.; Kandambeth, S.; Eddaoudi, M.; Alshareef, H.N. Layered Mg X V₂O₅· N H₂O as Cathode Material for High-Performance Aqueous Zinc Ion Batteries. *ACS Energy Lett.* **2018**, *3*, 2602–2609. [[CrossRef](#)]
23. Wang, Z.-T.; Wang, R.-C.; Tang, L.-B.; Li, Y.-J.; Mao, J.; Dai, K.-H.; He, Z.-J.; Zheng, J.-C. A Sandwich-Like Ti₃C₂@ Vo₂ Composite Synthesized by a Hydrothermal Method for Lithium Storage. *Solid State Ion.* **2021**, *369*, 115714. [[CrossRef](#)]
24. Wang, P.; Zhang, X.; Zhou, Y.; Jiang, Q.; Ye, Q.; Chu, Z.; Li, X.; Yang, X.; Yin, Z.; You, J. Solvent-Controlled Growth of Inorganic Perovskite Films in Dry Environment for Efficient and Stable Solar Cells. *Nat. Commun.* **2018**, *9*, 2225. [[CrossRef](#)] [[PubMed](#)]
25. Tan, Z.-K.; Moghaddam, R.S.; Lai, M.L.; Docampo, P.; Higler, R.; Deschler, F.; Price, M.; Sadhanala, A.; Pazos, L.M.; Credgington, D. Bright Light-Emitting Diodes Based on Organometal Halide Perovskite. *Nat. Nanotechnol.* **2014**, *9*, 687–692. [[CrossRef](#)] [[PubMed](#)]
26. Xia, H.-R.; Li, J.; Sun, W.-T.; Peng, L.-M. Organohalide Lead Perovskite Based Photodetectors with Much Enhanced Performance. *Chem. Commun.* **2014**, *50*, 13695–13697. [[CrossRef](#)]
27. Dou, L.; Yang, Y.M.; You, J.; Hong, Z.; Chang, W.-H.; Li, G.; Yang, Y. Solution-Processed Hybrid Perovskite Photodetectors with High Detectivity. *Nat. Commun.* **2014**, *5*, 5404. [[CrossRef](#)]
28. Zhang, Q.; Ha, S.T.; Liu, X.; Sum, T.C.; Xiong, Q. Room-Temperature near-Infrared High-Q Perovskite Whispering-Gallery Planar Nanolasers. *Nano Lett.* **2014**, *14*, 5995–6001. [[CrossRef](#)]
29. De Bastiani, M.; Saidaminov, M.I.; Dursun, I.; Sinatra, L.; Peng, W.; Buttner, U.; Mohammed, O.F.; Bakr, O.M. Thermochromic Perovskite Inks for Reversible Smart Window Applications. *Chem. Mater.* **2017**, *29*, 3367–3370. [[CrossRef](#)]
30. Kostopoulou, A.; Kymakis, E.; Stratakis, E. Perovskite Nanostructures for Photovoltaic and Energy Storage Devices. *J. Mater. Chem. A* **2018**, *6*, 9765–9798. [[CrossRef](#)]
31. Xia, H.-R.; Sun, W.-T.; Peng, L.-M. Hydrothermal Synthesis of Organometal Halide Perovskites for Li-Ion Batteries. *Chem. Commun.* **2015**, *51*, 13787–13790. [[CrossRef](#)]
32. Jaffe, A.; Karunadasa, H.I. Lithium Cycling in a Self-Assembled Copper Chloride–Polyether Hybrid Electrode. *Inorg. Chem.* **2014**, *53*, 6494–6496. [[CrossRef](#)]
33. Lira-Cantú, M.; Gómez-Romero, P. Electrochemical and Chemical Syntheses of the Hybrid Organic–Inorganic Electroactive Material Formed by Phosphomolybdate and Polyaniline. Application as Cation-Insertion Electrodes. *Chem. Mater.* **1998**, *10*, 698–704. [[CrossRef](#)]
34. Pal, P.; Ghosh, A. Three-Dimensional Cs Pb Cl₃ Perovskite Anode for Quasi-Solid-State Li-Ion and Dual-Ion Batteries: Mechanism of Li⁺ Conversion Process in Perovskite. *Phys. Rev. Appl.* **2020**, *14*, 064010. [[CrossRef](#)]
35. Pandey, P.; Sharma, N.; Panchal, R.A.; Gosavi, S.; Ogale, S. Realization of High Capacity and Cycling Stability in Pb-Free a₂CuBr₄ (a = Ch 3 Nh 3/Cs, 2d/3d) Perovskite-Based Li-Ion Battery Anodes. *ChemSusChem* **2019**, *12*, 3742–3746. [[CrossRef](#)] [[PubMed](#)]
36. Kostopoulou, A.; Vernardou, D.; Makri, D.; Brintakis, K.; Savva, K.; Stratakis, E. Highly Stable Metal Halide Perovskite Microcube Anodes for Lithium-Air Batteries. *J. Power Sources Adv.* **2020**, *3*, 100015. [[CrossRef](#)]
37. Kostopoulou, A.; Vernardou, D.; Savva, K.; Stratakis, E. All-Inorganic Lead Halide Perovskite Nanohexagons for High Performance Air-Stable Lithium Batteries. *Nanoscale* **2019**, *11*, 882–889. [[CrossRef](#)] [[PubMed](#)]
38. Kaiser, N.; Singh, A.; Yang, P.-Y.; Chen, Y.-T.; Li, S.; Pao, C.-W.; Jou, S.; Chu, C.-W. Long-Lifespan Lithium–Metal Batteries Obtained Using a Perovskite Intercalation Layer to Stabilize the Lithium Electrode. *J. Mater. Chem. A* **2020**, *8*, 9137–9145. [[CrossRef](#)]
39. Su, K.; Chi, P.; Paul, T.; Chung, C.; Chen, W.; Su, Y.; Wu, P.; Su, C.; Wu, M. Lithiation and Delithiation Induced Magnetic Switching and Electrochemical Studies in A-LifeO₂ Based Li Ion Battery. *Mater. Today Phys.* **2021**, *18*, 100373. [[CrossRef](#)]
40. Paul, T.; Chi, P.; Wu, P.M.; Wu, M. Computation of Distribution of Relaxation Times by Tikhonov Regularization for Li Ion Batteries: Usage of L-Curve Method. *Sci. Rep.* **2021**, *11*, 12624. [[CrossRef](#)]
41. Susai, F.A.; Talianker, M.; Liu, J.; Paul, T.; Grinblat, Y.; Erickson, E.; Noked, M.; Burstein, L.; Frenkel, A.I.; Tsur, Y. Electrochemical Activation of Li₂MnO₃ Electrodes at 0° C and Its Impact on the Subsequent Performance at Higher Temperatures. *Materials* **2020**, *13*, 4388. [[CrossRef](#)] [[PubMed](#)]
42. Paul, T. Modeling of the Impedance Data of Gadolinia Doped Ceria Based Actuators: A Distribution Function of Relaxation Times and Machine Learning Approach. *J. Phys. D Appl. Phys.* **2020**, *53*, 415503. [[CrossRef](#)]
43. Mishuk, E.; Ushakov, A.; Makagon, E.; Cohen, S.R.; Wachtel, E.; Paul, T.; Tsur, Y.; Shur, V.Y.; Kholkin, A.; Lubomirsky, I. Electro-Chemomechanical Contribution to Mechanical Actuation in Gd-Doped Ceria Membranes. *Adv. Mater. Interfaces* **2019**, *6*, 1801592. [[CrossRef](#)]
44. Paul, T.; Tsur, Y. Effect of Isovalent Doping on Grain Boundary Conductivity for La₂Mo₂O₉ Oxide Ion Conductor: A Distribution Function of Relaxation Times Approach. *Solid State Ion.* **2018**, *323*, 37–43. [[CrossRef](#)]

45. Paul, T.; Tsur, Y. Influence of Isovalent 'W' substitutions on the Structure and Electrical Properties of La₂Mo₂O₉ Electrolyte for Intermediate-Temperature Solid Oxide Fuel Cells. *Ceramics* **2021**, *4*, 502–515. [[CrossRef](#)]
46. Rodríguez-Carvajal, J. Recent Advances in Magnetic Structure Determination by Neutron Powder Diffraction. *Phys. B* **1993**, *192*, 55–69. [[CrossRef](#)]
47. Momma, K.; Izumi, F. Vesta 3 for Three-Dimensional Visualization of Crystal, Volumetric and Morphology Data. *J. Appl. Crystallogr.* **2011**, *44*, 1272–1276. [[CrossRef](#)]
48. Chiromawa, I.M.; Shaari, A.; Razali, R.; Ahams, S.T.; Abdullahi, M. Ab Initio Investigation of the Structure and Electronic Properties of Normal Spinel Fe₂SiO₄. *Malays. J. Fundam. Appl. Sci.* **2021**, *17*, 195–201. [[CrossRef](#)]
49. Giannozzi, P.; Andreussi, O.; Brumme, T.; Bunau, O.; Nardelli, M.B.; Calandra, M.; Car, R.; Cavazzoni, C.; Ceresoli, D.; Cococcioni, M. Advanced Capabilities for Materials Modelling with Quantum Espresso. *J. Phys. Condens. Matter* **2017**, *29*, 465901. [[CrossRef](#)]
50. Yadav, S.; Grinberg, I. First-Principles Study of the Composition, Cation Arrangement, and Local Structure in High-Performance Bi (Me 3+) O₃-Pb₁₀3 (Me 3+= Ga, Sc, in) Ferroelectric Solid Solutions. *J. Appl. Phys.* **2021**, *129*, 174101. [[CrossRef](#)]
51. Lai, M.; Kong, Q.; Bischak, C.G.; Yu, Y.; Dou, L.; Eaton, S.W.; Ginsberg, N.S.; Yang, P. Structural, Optical, and Electrical Properties of Phase-Controlled Cesium Lead Iodide Nanowires. *Nano Res.* **2017**, *10*, 1107–1114. [[CrossRef](#)]
52. Marronnier, A.; Roma, G.; Boyer-Richard, S.; Pedesseau, L.; Jancu, J.-M.; Bonnassieux, Y.; Katan, C.; Stoumpos, C.C.; Kanatzidis, M.G.; Even, J. Anharmonicity and Disorder in the Black Phases of Cesium Lead Iodide Used for Stable Inorganic Perovskite Solar Cells. *ACS Nano* **2018**, *12*, 3477–3486. [[CrossRef](#)]
53. Wang, K.; Jin, Z.; Liang, L.; Bian, H.; Bai, D.; Wang, H.; Zhang, J.; Wang, Q.; Liu, S. All-Inorganic Cesium Lead Iodide Perovskite Solar Cells with Stabilized Efficiency Beyond 15%. *Nat. Commun.* **2018**, *9*, 4544. [[CrossRef](#)] [[PubMed](#)]
54. Liu, X.; Tang, Z.; Li, Q.; Zhang, Q.; Yu, X.; Gu, L. Symmetry-Induced Emergent Electrochemical Properties for Rechargeable Batteries. *Cell Rep. Phys. Sci.* **2020**, 100066. [[CrossRef](#)]
55. Jiang, Q.; Chen, M.; Li, J.; Wang, M.; Zeng, X.; Besara, T.; Lu, J.; Xin, Y.; Shan, X.; Pan, B. Electrochemical Doping of Halide Perovskites with Ion Intercalation. *ACS Nano* **2017**, *11*, 1073–1079. [[CrossRef](#)] [[PubMed](#)]
56. Illig, J.; Ender, M.; Chrobak, T.; Schmidt, J.P.; Klotz, D.; Ivers-Tiffée, E. Separation of Charge Transfer and Contact Resistance in LiFePO₄-Cathodes by Impedance Modeling. *J. Electrochem. Soc.* **2012**, *159*, A952. [[CrossRef](#)]
57. Lu, H.; Guo, Q.; Fan, Q.; Xue, L.; Lu, X.; Zan, F.; Xia, H. Cobalt Sulfide Quantum Dot Embedded in Nitrogen/Sulfur-Doped Carbon Nanosheets as a Polysulfide Barrier in Li-S Batteries. *J. Alloy. Compd.* **2021**, *870*, 159341. [[CrossRef](#)]
58. Brik, M.; Kityk, I.; Denysyuk, N.; Khyzhun, O.; Levkovets, S.; Parasyuk, O.; Fedorchuk, A.; Myronchuk, G. Specific Features of the Electronic Structure of a Novel Ternary Tl₃Pb₅ Optoelectronic Material. *Phys. Chem. Chem. Phys.* **2014**, *16*, 12838–12847. [[CrossRef](#)]
59. Zhang, M.; Tian, Z.-Q.; Zhu, D.-L.; He, H.; Guo, S.-W.; Chen, Z.-L.; Pang, D.-W. Stable CsPbBr₃ Perovskite Quantum Dots with High Fluorescence Quantum Yields. *New J. Chem.* **2018**, *42*, 9496–9500. [[CrossRef](#)]
60. Ziv, B.; Borgel, V.; Aurbach, D.; Kim, J.-H.; Xiao, X.; Powell, B.R. Investigation of the Reasons for Capacity Fading in Li-Ion Battery Cells. *J. Electrochem. Soc.* **2014**, *161*, A1672. [[CrossRef](#)]
61. Momose, H.; Honbo, H.; Takeuchi, S.; Nishimura, K.; Horiba, T.; Muranaka, Y.; Kozono, Y.; Miyadera, H. X-Ray Photoelectron Spectroscopy Analyses of Lithium Intercalation and Alloying Reactions on Graphite Electrodes. *J. Power Sources* **1997**, *68*, 208–211. [[CrossRef](#)]
62. Wang, Q.; Yang, T.; Wang, H.; Zhang, J.; Guo, X.; Yang, Z.; Lu, S.; Qin, W. Morphological and Chemical Tuning of Lead Halide Perovskite Mesocrystals as Long-Life Anode Materials in Lithium-Ion Batteries. *CrystEngComm* **2019**, *21*, 1048–1059. [[CrossRef](#)]
63. Martos, M.; Morales, J.; Sanchez, L. Lead-Based Systems as Suitable Anode Materials for Li-Ion Batteries. *Electrochim. Acta* **2003**, *48*, 615–621. [[CrossRef](#)]
64. Han, T.H.; Lee, J.W.; Choi, Y.J.; Choi, C.; Tan, S.; Lee, S.J.; Zhao, Y.; Huang, Y.; Kim, D.; Yang, Y. Surface-2d/Bulk-3d Heterophased Perovskite Nanograins for Long-Term-Stable Light-Emitting Diodes. *Adv. Mater.* **2020**, *32*, 1905674. [[CrossRef](#)]
65. Yue, L.; Tang, J.; Li, F.; Xu, N.; Zhang, F.; Zhang, Q.; Guan, R.; Hong, J.; Zhang, W. Enhanced Reversible Lithium Storage in Ultrathin W₁₈O₄₉ Nanowires Entwined Si Composite Anode. *Mater. Lett.* **2017**, *187*, 118–122. [[CrossRef](#)]
66. Chen, Z.; Ye, K.; Li, M.; Zhao, S.; Luo, J.; Wu, B. Lithiation Mechanism of W₁₈O₄₉ Anode Material for Lithium-Ion Batteries: Experiment and First-Principles Calculations. *J. Electroanal. Chem.* **2021**, *880*, 114885. [[CrossRef](#)]
67. Smith, A.; Dahn, J. Delta Differential Capacity Analysis. *J. Electrochem. Soc.* **2012**, *159*, A290. [[CrossRef](#)]
68. Korthauer, R. *Lithium-Ion Batteries: Basics and Applications*; Springer: Berlin, Germany, 2018.
69. Zhang, Y.; Wang, N.; Bai, Z. The Progress of Cobalt-Based Anode Materials for Lithium Ion Batteries and Sodium Ion Batteries. *Appl. Sci.* **2020**, *10*, 3098. [[CrossRef](#)]
70. Liu, Y.; Zhang, L.; Zhao, Y.; Shen, T.; Yan, X.; Yu, C.; Wang, H.; Zeng, H. Novel Plasma-Engineered MoS₂ Nanosheets for Superior Lithium-Ion Batteries. *J. Alloy. Compd.* **2019**, *787*, 996–1003. [[CrossRef](#)]
71. Wang, P.; Tian, J.; Hu, J.; Zhou, X.; Li, C. Supernormal Conversion Anode Consisting of High-Density MoS₂ Bubbles Wrapped in Thin Carbon Network by Self-Sulfuration of Polyoxometalate Complex. *ACS Nano* **2017**, *11*, 7390–7400. [[CrossRef](#)]
72. Tang, J.; Lugo, C.E.Z.; Guzmán, S.F.A.; Daniel, G.; Kessler, V.G.; Seisenbaeva, G.A.; Pol, V.G. Pushing the Theoretical Capacity Limits of Iron Oxide Anodes: Capacity Rise of Fe₂O₃ Nanoparticles in Lithium-Ion Batteries. *J. Mater. Chem. A* **2016**, *4*, 18107–18115. [[CrossRef](#)]

-
73. Hassan, M.F.; Guo, Z.; Chen, Z.; Liu, H. A-Fe₂O₃ as an Anode Material with Capacity Rise and High Rate Capability for Lithium-Ion Batteries. *Mater. Res. Bull.* **2011**, *46*, 858–864. [[CrossRef](#)]
 74. An, S.J.; Li, J.; Daniel, C.; Mohanty, D.; Nagpure, S.; Wood III, D.L. The State of Understanding of the Lithium-Ion-Battery Graphite Solid Electrolyte Interphase (Sei) and Its Relationship to Formation Cycling. *Carbon* **2016**, *105*, 52–76. [[CrossRef](#)]